ADVANCED MATERIALS
www.advmat.de

Substitutional p-Type Doping in NbS_2–MoS_2 Lateral Heterostructures Grown by MOCVD

*Zhenyu Wang, Mukesh Tripathi, Zahra Golsanamlou, Poonam Kumari, Giuseppe Lovarelli, Fabrizio Mazziotti, Demetrio Logoteta, Gianluca Fiori, Luca Sementa, Guilherme Migliato Marega, Hyun Goo Ji, Yanfei Zhao, Aleksandra Radenovic, Giuseppe Iannaccone, Alessandro Fortunelli, and Andras Kis**

Monolayer MoS_2 has attracted significant attention owing to its excellent performance as an n-type semiconductor from the transition metal dichalcogenide (TMDC) family. It is however strongly desired to develop controllable synthesis methods for 2D p-type MoS_2, which is crucial for complementary logic applications but remains difficult. In this work, high-quality NbS_2–MoS_2 lateral heterostructures are synthesized by one-step metal–organic chemical vapor deposition (MOCVD) together with monolayer MoS_2 substitutionally doped by Nb, resulting in a p-type doped behavior. The heterojunction shows a p-type transfer characteristic with a high on/off current ratio of ≈10^4, exceeding previously reported values. The band structure through the NbS_2–MoS_2 heterojunction is investigated by density functional theory (DFT) and quantum transport simulations. This work provides a scalable approach to synthesize substitutionally doped TMDC materials and provides an insight into the interface between 2D metals and semiconductors in lateral heterostructures, which is imperative for the development of next-generation nanoelectronics and highly integrated devices.

1. Introduction

Semiconducting 2D transition metal dichalcogenides (TMDCs) have been extensively investigated for next-generation nanoelectronics and optoelectronics because of their atomic scale thickness,[1] layer-dependent band structure,[2] and favorable electrical properties.[3] Among them, monolayer molybdenum disulfide (MoS_2) is most widely studied due to its strong photoluminescence[4] (PL) and high stability.[3] Monolayer MoS_2 with a large intrinsic bandgap of 1.8 eV[5] and a high on/off current ratio of 10^8 in n-type FET devices[1] behaves as an n-type semiconductor, which is attributed to the electron doping by sulfur vacancies,[6,7] Moreover, MoS_2-based integrated nanoelectronics are emerging rapidly in recent years, such as in-memory devices[8] and artificial neural networks (ANNs),[9] which highlights their potential to extend Moore's law in advanced technologies.[10,11] Complementary logic applications based on MoS_2 are desirable for the realization of a platform for low energy-consuming and high effective computing, which requires the reliable synthesis of p-type MoS_2.[12]

Several methods have been reported to achieve p-type doped MoS_2, such as plasma treatment,[13–15] charge transfer,[16,17] and contact engineering.[12,17] However, these non-intrinsic p-type doped MoS_2 were limited to multilayer thicknesses and their further applications are hindered by the complicated process

Z. Wang, M. Tripathi, G. M. Marega, H. G. Ji, Y. Zhao, A. Kis
Electrical Engineering Institute
École Polytechnique Fédérale de Lausanne (EPFL)
Lausanne CH-1015, Switzerland
E-mail: andras.kis@epfl.ch

Z. Wang, M. Tripathi, G. M. Marega, H. G. Ji, Y. Zhao, A. Kis
Institute of Materials Science and Engineering
École Polytechnique Fédérale de Lausanne (EPFL)
Lausanne CH-1015, Switzerland

The ORCID identification number(s) for the author(s) of this article can be found under https://doi.org/10.1002/adma.202209371.

DOI: 10.1002/adma.202209371

Z. Golsanamlou, P. Kumari, L. Sementa, A. Fortunelli
CNR-ICCOM and IPCF
Consiglio Nazionale delle Ricerche
via G. Moruzzi 1, Pisa I-56124, Italy

G. Lovarelli, F. Mazziotti, D. Logoteta, G. Fiori, G. Iannaccone
Department of Information Engineering
Università di Pisa
Pisa I-56122, Italy

G. Lovarelli
Department of Physics "E. Fermi"
Università di Pisa
Pisa I-56127, Italy

A. Radenovic
Institute of Bioengineering
École Polytechnique Fédérale de Lausanne (EPFL)
Lausanne CH-1015, Switzerland

and low controllability,[18] showing that the synthesis of high-quality and controllable p-type doped monolayer MoS_2 remains a challenge. Recently, some attempts have been reported to introduce substitutional metal doping with Nb atoms inside MoS_2 lattice structure by chemical vapor deposition (CVD),[18–20] realizing charge transfer by electron occupation of metal d-orbitals.[21,22] Nevertheless, these p-type MoS_2 FET devices show a low on/off ratio and carrier mobility because of their large contact resistance related to strong Fermi level pinning on metal contacts.

2D metal–semiconductor (M–S) junctions based on TMDC heterostructures are expected to result in a reduced contact resistance due to weakened Fermi level pinning and modulation of the Schottky barrier.[23] Furthermore, the interface of these 2D M–S heterostructures is one of the crucial factors determining their performance, requiring comprehensive characterization, such as identifying geometrical distortions, interfacial coupling, and electronic states.[24] Although TMDC heterostructures can be obtained using the transfer technique thanks to van der Waals interactions,[25] CVD growth is scalable toward large area growth, layer number control, high reproducibility, as well as low residue[26] concentration. Several examples of lateral and vertical TMDC heterostructures grown by CVD have been reported, including semiconductor–semiconductor heterostructures (e.g., MoS_2/WS_2,[27] $MoS_2/MoSe_2$[28]) and metal–semiconductor heterostructures (e.g., NbS_2/WS_2[29]).

Here, we demonstrate the one-step simultaneous MOCVD synthesis of NbS_2–MoS_2 lateral heterostructures with p-type Nb substitutional doping of monolayer MoS_2. Atomic force microscopy (AFM), Raman spectroscopy, photoluminescence (PL), aberration-corrected scanning transmission electron microscopy (STEM) combined with energy-dispersive X-ray spectroscopy (EDX) were used to confirm the high-quality lateral heterostructure growth and substitutional Nb doping. The FET device based on our heterojunction exhibits a p-type transfer characteristic with the highest on/off current ratio of 10^4 ever reported in p-type MoS_2 realized via substitutional metal doping. Density-functional theory (DFT) simulations were performed to calculate the band structures of Nb-doped MoS_2 and reveal the Fermi level alignment at the interface with the critical role of doping. Temperature-dependent *I–V* characterization and self-consistent quantum transport simulations were carried out to extract the Schottky barrier height (SBH) at the interface of the p-type heterojunction.

2. Results and Discussion

2.1. 2D NbS_2–MoS_2 Lateral Heterostructures Grown by MOCVD

Our NbS_2–MoS_2 lateral heterostructures were synthesized by sequentially growing each component on a *c*-plane sapphire wafer in a home-built MOCVD system, as schematically shown on **Figure 1**a. Since NbS_2 requires a higher growth temperature than MoS_2 according to our previous results,[30,31] the quartz tube was first heated to 850 °C with temperature maintained for 10 min for monolayer MoS_2 growth. During this time, molybdenum hexacarbonyl ($Mo(CO)_6$) and hydrogen sulfide (H_2S) precursors were simultaneously introduced into the growth tube. Subsequently, the precursor supply was turned off and the tube was continuously heated until 950 °C. Monolayer MoS_2 on sapphire substrate was in turn employed for the preparation of heterostructures. H_2S flow was resumed, reacting with the pre-coated $NbCl_5$ and resulting in NbS_2 growth. Initial nucleation of NbS_2 preferably takes place at the edges of as-grown MoS_2 due to its high chemical reactivity. NbS_2 growth continues outward onto the surface of sapphire owing to its lower Gibbs free energy compared to the surface of MoS_2,[32] resulting in lateral NbS_2–MoS_2 heterostructures. Typical as-grown NbS_2–MoS_2 lateral heterostructures are shown in Figure 1b, characterized by MoS_2 triangles with a lateral size of ≈30 µm and surrounded by NbS_2 with a width of ≈5 µm. Notably, the successive growth of both components without air exposure prevents the oxidation of as-grown MoS_2 edges, which is essential for the formation of high-quality lateral heterostructures. Additional details on the growth method are available in the Experimental Section.

Figure 1c shows the AFM image of an as-grown NbS_2–MoS_2 lateral heterostructure on the sapphire substrate, indicating a smooth surface with a thickness of 3 nm for NbS_2 and a height of 0.7 nm for monolayer MoS_2. By controlling the different growth parameters, we were able to tune the thickness of NbS_2 within the heterostructures between 3 and 10 nm. Figure 1d presents the Raman spectra obtained from different regions of the heterostructure acquired at room temperature. The Raman spectrum from the central region (orange curve) contains two typical peaks at 383 cm^{-1} (E^1_{2g}) and 402 cm^{-1} (A_{1g}), confirming the monolayer nature of MoS_2. The peripheral region shows peaks in the Raman spectrum (red curve) located at 340 cm^{-1} (E^1_{2g}) and 379 cm^{-1} (A_{1g}), in agreement with the vibration modes of NbS_2. Raman intensity maps corresponding to the characteristic modes of NbS_2 and MoS_2 are shown in Figure 1e. Uniform signals indicate uniform chemical distribution and the clear boundaries can be seen between the NbS_2 and MoS_2 regions, confirming the formation of in-plane heterostructures without alloying.

To investigate the atomic structure and interface of the heterostructure, aberration-corrected annular dark-field (ADF)-STEM imaging was performed with images shown in Figure 1f,g. Due to varying thickness, few-layer NbS_2 shows stronger contrast in comparison to monolayer MoS_2. The magnified and filtered image shows a clear and sharp interface between the two materials. Moreover, the fact that NbS_2 is vertically stacked in a hexagonal lattice arrangement (2H-phase) with no visible defects in the individual regions suggests a high crystalline quality of our heterostructure samples. A relative orientation angle of ≈30° is estimated from their atomic lattice structure of the heterostructure, which can be further confirmed from the corresponding fast Fourier transformation (FFT) image shown in the inset. Energy-dispersive X-ray spectrometry (EDX) spectrum and mappings shown in Figure S1 (Supporting Information) present the elemental spatial distribution, also confirming the chemical compositions of NbS_2 and MoS_2. Geometric phase analysis (GPA) of the corresponding ADF-STEM image shows compressive in-plane strain along the interface with MoS_2 (see Figure 1h). Distribution of strain is clearly observed along the interface, which is attributed to the lattice mismatch and layer variations of the two compounds.

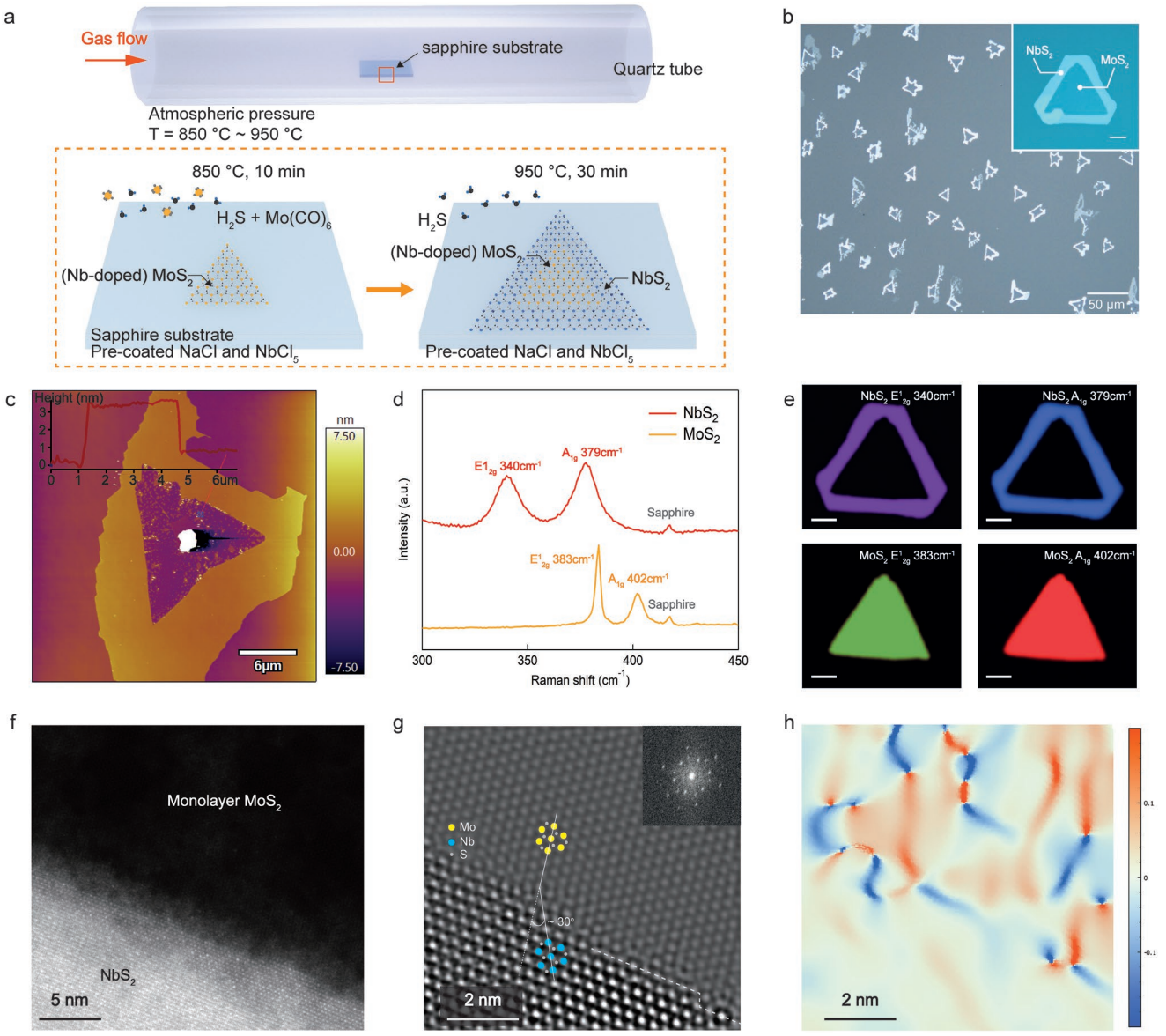

Figure 1. NbS_2–MoS_2 lateral heterostructures grown by MOCVD. a) Schematic illustration of the MOCVD process for NbS_2–MoS_2 lateral heterostructure growth. b) Optical microscopy image of as-grown NbS_2–MoS_2 lateral heterostructures grown on sapphire. Inset: Zoomed-in image presenting a MoS_2 triangle surrounded by NbS_2. Scale bar: 10 μm. c) AFM image and the corresponding height profile of as-grown NbS_2–MoS_2 lateral heterostructure. The thicknesses of NbS_2 and MoS_2 are ≈3 nm and 0.7 nm, respectively. d) Raman spectra at room temperature for NbS_2–MoS_2 lateral heterostructures on sapphire. The red curve was measured on peripheral NbS_2, while the orange curve was taken on central MoS_2. e) Raman mapping images based on the intensity of the typical modes on NbS_2 region and MoS_2 region from the heterostructure sample. Scale bar: 10 μm. f,g) STEM images taken on the interface of NbS_2–MoS_2 lateral heterostructure. The darker side shows monolayer MoS_2, while the brighter sides correspond to few-layer NbS_2. A mis-orientation angle of 30° can be observed. Inset of (g) FFT of the ADF-STEM image shown in (g). The separated diffraction spots indicate the in-plane growth of the heterostructure. h) 2D strain mapping of NbS_2–MoS_2 heterostructure for in-plane (ε_{xx}) direction, which is analysed from the corresponding image shown in (g).

2.2. p-Type Nb-Doped Monolayer MoS_2 in the Heterostructures

Our monolayer MoS_2 in the heterostructures was substitutionally doped with Nb atoms during the MOCVD process. Nb dopants were introduced from pre-coated $NbCl_5$ into the MoS_2 lattice during the initial, MoS_2 growth phase, at 850 °C (Figure 1a, left panel). Notably, the substitutional doping (together with MoS_2 growth) and the formation of the heterostructure interface with NbS_2 and subsequent NbS_2 take place at different stages and temperatures of growth process, independently of each other.

A typical ADF-STEM image acquired in the individual MoS_2 region in Figure S2a (Supporting Information) shows the large and contamination-free region. Further magnified ADF-STEM image in **Figure 2**a shows the perfect atomic lattice structure of monolayer MoS_2. Several sulfur vacancies, a

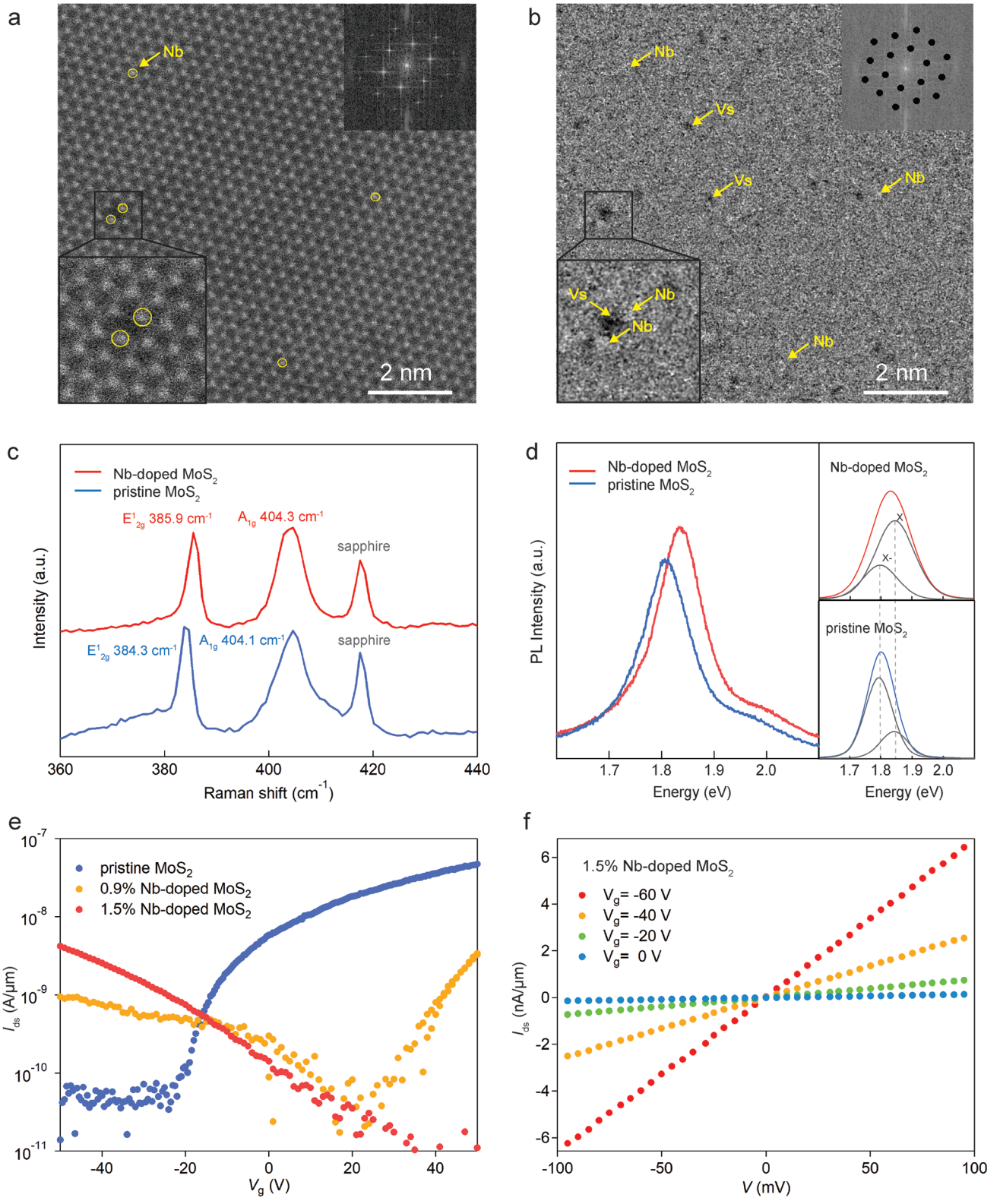

Figure 2. Nb-doped MoS_2 in the lateral heterostructures. a,b) ADF-STEM image of the Nb-doped MoS_2 film and inverse fast Fourier transform (IFFT) filtered image, respectively. Top-right insets show the corresponding FFT images. c,d) Raman and PL spectrum of Nb-doped MoS_2 compared with pristine MoS_2 on sapphire substrates measured at room temperature. e) Transport properties of Nb-doped MoS_2 with various doping concentrations. A Ti/Au stack is utilized as an electrode contact. Pristine MoS_2 shows an n-type behavior, 0.9% Nb-doped MoS_2 shows both p-type and n-type behavior, and 1.5% Nb-doped MoS_2 shows a p-type behavior. Source–drain voltage was fixed at 200 mV during the measurement. f) *I–V* curves of 1.5% Nb-doped MoS_2 under various back-gate voltages at room temperature.

common defect in TMDCs, can be observed. The fast Fourier transform (inset) pattern from the corresponding image further confirms the high-quality growth. In principle, different atoms can be identified directly from their atomic contrast because of the relation between ADF intensity and the Z number ($\approx Z^2$). However, since Nb and Mo differ from each other by only one Z number, it is not straightforward to distinguish them in ADF-STEM images. Therefore, the inverse fast Fourier transition (IFFT) method was used to identify Nb dopants in MoS_2,[33] as shown in Figure 2b. Nb atoms are highlighted with yellow circles in Figure 2a and can be seen as bright dots at the corresponding location in Figure 2b. Sulfur vacancies (V_S) are also visible as black dots in Figure 2b. Quantitative ADF-STEM simulations were also performed to distinguish Nb as substituent atoms (see in Figure S2c, Supporting Information), using the DFT calculated atomic models with similar imaging parameters as in the experiments. The line profiles from both experimental and simulated images show a lower intensity along Nb atoms compared with Mo atoms. In addition, to extract the doping concentration precisely, EDX spectroscopy was further employed in the MoS_2 region as shown in Figure S3 (Supporting Information). Elemental mapping and spectrum from the corresponding region show the spatial distribution of S, Mo, and Nb atoms. Although the K and L edge energies for Nb and Mo are very close, peak deconvolution can be used to separate them, highlighting the uniform distribution of the three elements within the measured region showing an atomic concentration of S > Mo > Nb. Average Nb dopant concentration extracted from the EDX is ≈1.5%.

Figure 2c compares Raman spectra acquired from the Nb-doped MoS_2 and pristine MoS_2 on sapphire substrate. Both of the characteristic peaks (E^1_{2g} and A_{1g}) show a separation of ≈20 cm^{-1}, indicating the monolayer nature of the pristine MoS_2 and Nb-doped MoS_2. The Raman signals of Nb-doped MoS_2 show a blueshift compared with the pristine MoS_2, consistent with previous literature.[18] The same location of sapphire signals confirms that the shift is not due to noise. The shift of Raman spectra depends on the coexistence of strain and charge doping.[34,35] In our case, the blueshift of Raman signals can be explained by growth-induced tensile strain and reduced electron-phonon scattering, which results from the distorted lattice and hole injection due to the substitutional Nb-doping,[18] respectively.

Figure 2d presents PL spectra of Nb-doped monolayer MoS_2 and pristine monolayer MoS_2, as well as their corresponding fitting curves. A strong PL peak located at ≈1.80 eV was observed in pristine monolayer MoS_2, in-line with its direct-bandgap nature.[4] Compared with pristine MoS_2, the Nb-doped monolayer MoS_2 shows a blueshifted PL peak with enhanced intensity, which is consistent with previous results on p-type doping of MoS_2,[18,36] To explain the spectral changes, the PL peaks can be considered as a combination of the trion (X^-) peak at ≈1.79 eV and the exciton (X) peak at ≈1.85 eV, as shown by the gray curves. In pristine MoS_2, the PL spectra are dominated by the trion (X^-) peak because of the strong electron doping.[37] With Nb doping, the exciton (X) peak becomes dominant due to the reduced electron density and a suppressed electron concentration.

To examine electrical transport properties of our Nb-doped MoS_2, transfer characteristics were studied on multiple samples with different doping concentrations with results shown in Figure 2e. Notably, a Ti/Au stack was used as a conventional 3D contact to our MoS_2 channel. The variation of Nb dopant concentration is due to different amounts of spin-coated $NbCl_5$ precursor during growth, which shows a range of 0.9% to 4.6% according to our EDX analysis (see in Figure S4, Supporting Information). A clear transition from n-type to p-type is visible from the transfer curves, as the Nb dopant concentration increases. In 1.5% Nb-doped MoS_2 sample, a typical p-type behavior with an on/off ratio of 1×10^3 and field-effect mobility of ≈1.43 $cm^2\ V^{-1}\ s^{-1}$ was observed. The mobility is lower than that of pristine MoS_2, which can be attributed to the increased structural distortion because of substitutional Nb doping in MoS_2. Nevertheless, in a sense of material development, p-type MoS_2 achieved by substitutional doping is already an advancement compared to pristine MoS_2. Additionally, a linear I–V curve displays ohmic contacts between Nb-doped MoS_2 and Ti electrodes within our measured range, as shown in Figure 2f.

2.3. Atomistic and Electronic Structures of NbS_2–MoS_2 Heterojunction

To shed theoretical insight into the heterojunction between metallic NbS_2 and p-type Nb-doped monolayer MoS_2, first-principle calculations were performed based on DFT. Density of states (DOS) and the band structure for the heterojunction are shown in **Figure 3**. The detailed calculation parameters are available in the Supporting Information.

To model the NbS_2–MoS_2 lateral heterostructure at the quantum-mechanical (QM) level, we exploit the virtual crystal approximation (VCA),[38] i.e., we define "mixed" chemical elements composed of a given percentage of Nb and Mo elements. This allows us to rapidly analyze the structural and electronic properties of phases with Mo/Nb mixed composition. From this analysis, we create our QM structural model: a reasonably large unit cell (depicted in Figure 3a) made of: i) pure NbS_2, ii) a Nb-doped MoS_2 buffer, and iii) a slightly Nb-doped core/pristine MoS_2 (the Nb-doping content is ≈1.5% at the experimental level, set to 1.66% for convenience in the simulations). The buffer phase (ii) is introduced to mediate the 5% lattice mismatch between MoS_2 (3.19 Å at the DFT level) and NbS_2 (3.35 Å). Its doping level is set to 8.3%, as this doping is energetically the most stable, i.e., it has the minimum gradient of total energy and work function with respect to the lattice parameter (see the Supporting Information for more details).

The VCA analysis of the pure phases detailed in the Supplementary Information confirms the dependence of band structure upon lattice parameters.[40,41] Moreover, a fragment analysis[39] of the system, illustrated in Figure 3e, leads us to two further conclusions. First, the top of the valence band (TVB) of semiconducting MoS_2 is pinned to the Fermi level of the system. Second, there are two localized barriers in the electrostatic potential at the NbS_2/[8.3%Nb-doped-MoS_2]/[1.7%Nb-doped-MoS_2] junctions of $\Delta_h \approx 72$ meV and

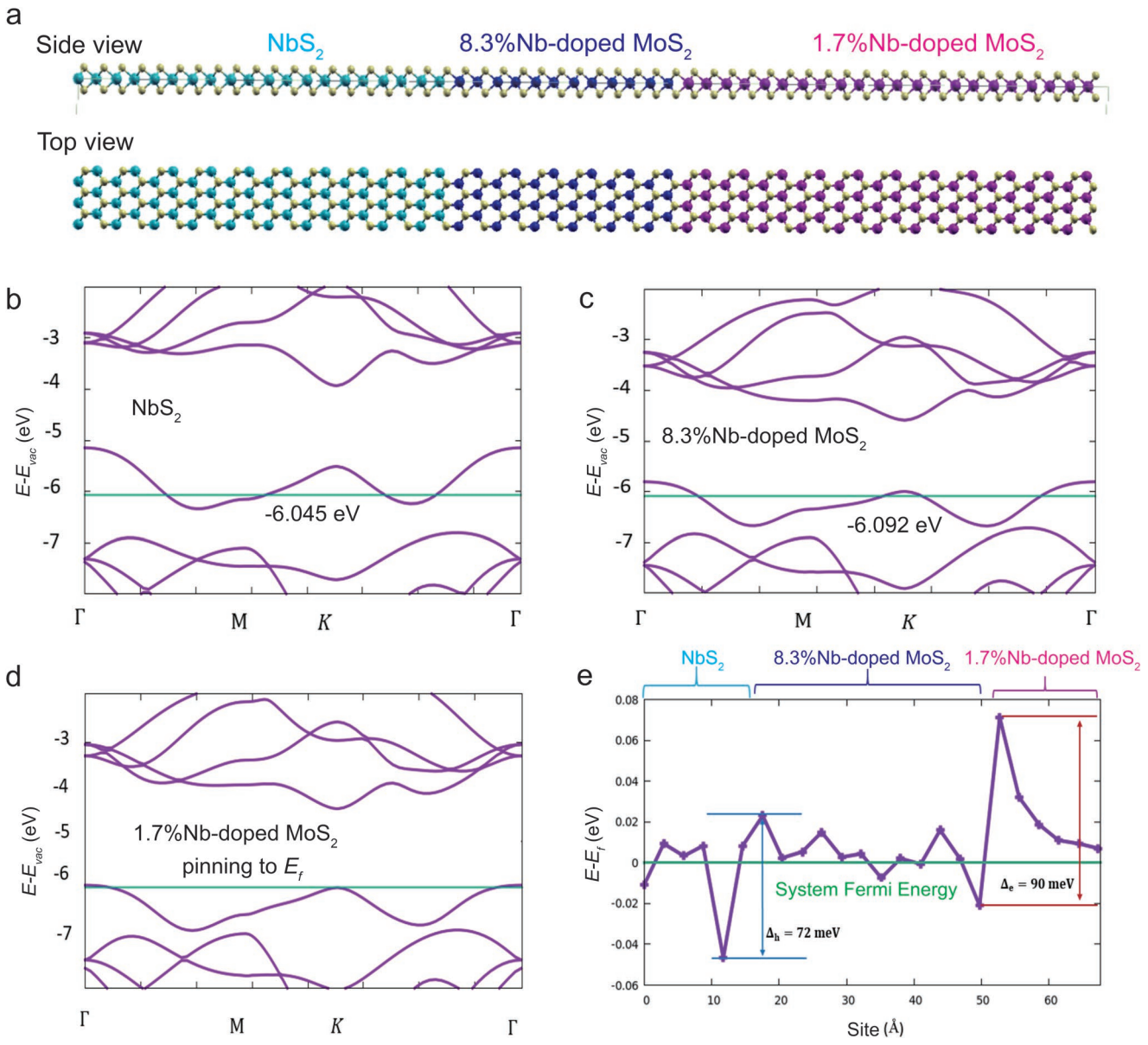

Figure 3. QM modeling of the NbS_2/MoS_2 lateral heterostructure in terms of a composite three-phase NbS_2/8.3% Nb-doped MoS_2/1.7% Nb-doped MoS_2 system. a) Atomistic depictions in side and top views. b–d) Band structure of the pure fragments, aligned as derived from the analysis of the electrostatic potential in the scattering system. e) Profile of local Fermi energy or local top of the valence band profile along the transmission direction derived from a fragment analysis of the electrostatic potential on metal atoms,[39] with a highlighted potential jump at the buffer-phase/MoS_2 junction of $\Delta = 90$ meV.

$\Delta_e \approx 90$ meV, which suggests a suppression of transmission at the heterojunctions, despite the uncertainty in the values of these barriers due to the deformation of the band structure following the formation of charge dipoles at the interface (Figure S11, Supporting Information). In synthesis, QM modeling predicts that the lattice and electronic mismatch at the NbS_2–MoS_2 lateral heterostructure is overcome by Nb doping of MoS_2 (as produced by growing NbS_2 in excess of Nb onto pre-prepared MoS_2 flakes and evidenced by EDX and ADF-STEM measurements) mediating structurally and electronically the $NbS_2 \rightarrow MoS_2$ transformation, and giving rise to a p-type NbS_2–MoS_2 heterojunction, also possessing good electrical transport properties.

2.4. p-Type NbS_2–MoS_2 Heterojunctions

To characterize the transport properties of our MOCVD-grown NbS_2/p-type MoS_2 lateral heterostructures, FET devices based on the heterojunctions were fabricated on Si/SiO_2 substrate (shown in Figure S5, Supporting Information), where NbS_2 is used as a 2D contact compared to the devices with conventional

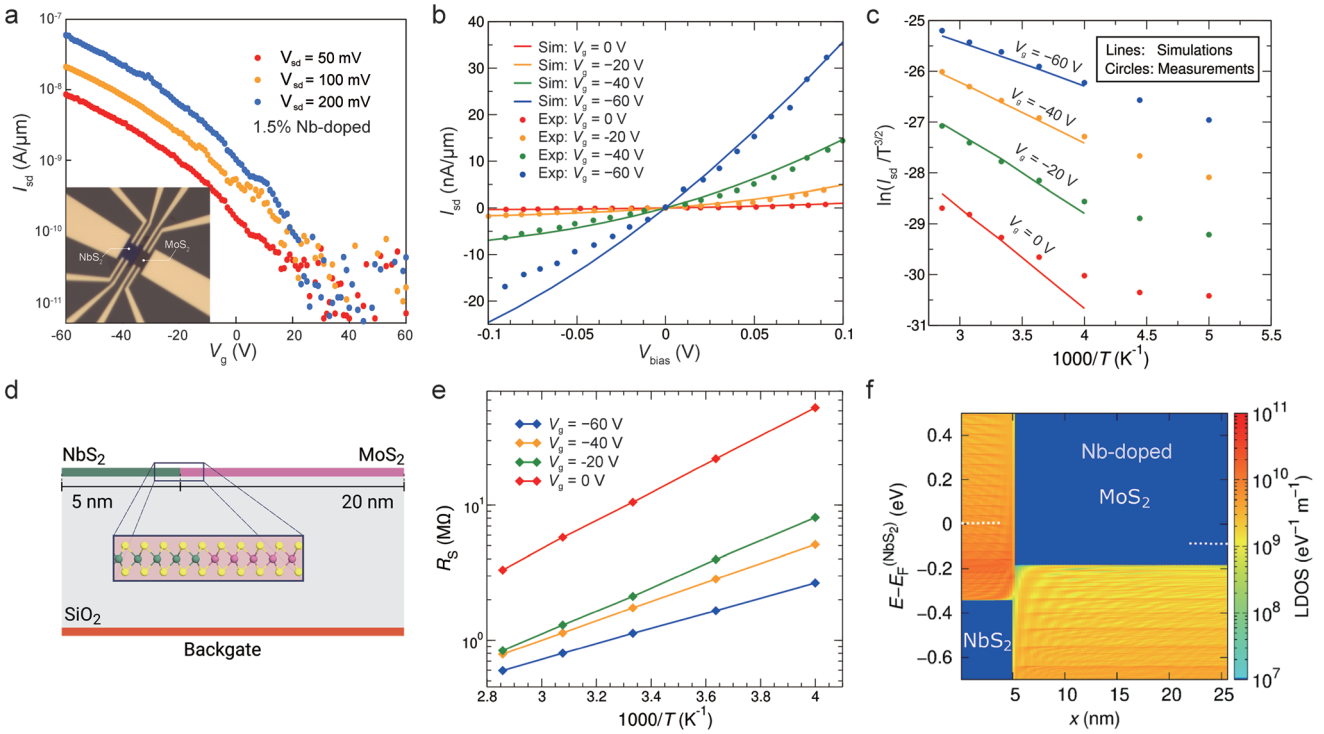

Figure 4. a) Room-temperature transfer characteristic of the FET device based on the NbS_2–MoS_2 lateral heterojunction with 1.5% of Nb doping concentration, shown in the inset. NbS_2 is utilized as a 2D contact. Scale bar: 10 μm. Back-gate voltage V_g is applied to the substrate with a source-to-drain voltage ranging from 50 to 200 mV. P-type behavior is demonstrated from the transfer curves. b) Comparison of measured and simulated I_{ds}–V characteristics of an NbS_2–MoS_2 lateral heterojunction at room temperature for different values of back-gate voltage. c) Comparison of the Arrhenius plots obtained from measurements (dots) and simulations (lines). The probe voltage was fixed to 100 mV during the measurement. d) Sketch of the simulated device (not to scale). e) Sheet resistance R_s extracted from simulations as a function of temperature. f) Colormap of the density of states along the device close to flat-band conditions. The dotted lines denote the Fermi level at the NbS_2 and MoS_2 contacts.

3D contacts shown in Figure 2e. A linear I–V curve confirms metallic behavior without gate modulation of our NbS_2 at room temperature with a total resistance (R_{tot}) of 770 Ω (see in Figure S6, Supporting Information). **Figure 4**a demonstrates the room-temperature transfer characteristic curves collected from the FET devices shown in the bottom-left image with a 1.5% Nb doping concentration. A typical p-type behavior with an on/off ratio of 1×10^4 was observed and the four-probe field-effect mobility is calculated to be 1.46 cm^2 V^{-1} s^{-1} (defined as $\mu = \frac{dI_{ds}}{dV_g} \times \frac{L}{WC_iV}$, where L and W are the channel length and width between two voltage probes, respectively, while C_i is the capacitance between Nb-doped MoS_2 channel and the back gate per unit area). The four-probe I–V curves in Figure 4b present the output characteristics of the NbS_2–MoS_2 lateral heterojunction at room temperature. A non-symmetric current rectification behavior is visible from the I–V curves, indicating the presence of a Schottky contact at the heterointerface. To study the Schottky barrier height (SBH) at the NbS_2/p-type MoS_2 junction, temperature-dependent transport measurements were carried out under various gate voltages, as shown in Figure 4c. In order to obtain an accurate estimate of the barrier height, we fit the measurement data with the results of quantum transport simulations of the heterojunction. We have used the following transport model to perform our simulation: NbS_2 and MoS_2 monolayers were described by a nearest-neighbor, two-orbital tight-binding Hamiltonian. The Hamiltonian parameters were calibrated to obtain the best agreement with the DFT band structures of the uncoupled materials in the energy range of interest for transport phenomena. This model leaves as free parameters the hopping amplitude between the monolayers at the heterointerface and the height of the Schottky barrier in flat-band conditions. The value of both of these quantities was iteratively adjusted in order to obtain the best fit of the I_{ds}–V characteristics. The value t_{IF} of the hopping amplitude considered in simulations also accounts for the cumulative effect of the defects and disorder localized at interface, which is otherwise assumed to be ideal in our model. We estimated $|t_{IF}| \approx 2 \times 10^{-6}$ eV, a very small value, which suggests a strongly defective interface in addition to the localized barriers already observed in Figure 3e.

The cross section of the simulated device is sketched in Figure 4d. The simulation domain in the transport direction is restricted to a neighborhood of the heterointerface. For a given I_{ds} current, the voltage drop over this region is smaller than the experimentally measured V, due to the presence of a residual parasitic sheet resistance R_s associated to the ≈5 μm-long MoS_2 region between the heterojunction and the voltage contact. In order to map the source-to-drain bias over the simulation region into V, and thus, obtain results directly

comparable with the experimental data, we estimated R_s from the I_{ds}–V measurements at room temperature by means of the Cheung method.[42] The dependence of R_s on the temperature was modeled by assuming $R_s \propto \exp\left(\frac{\Delta E_v}{k_B T}\right)$, where the distance ΔE_v between the top of the valence band and the Fermi level in the MoS_2 was estimated from the simulation of the metal/SiO_2/MoS_2 stack in equilibrium conditions. It is shown in Figure 4e for different values of V_g.

To take into account the substitutional doping due to Nb atoms, MoS_2 was assumed p-doped at a concentration of 6×10^{12} cm^{-2}. This value is in reasonable agreement with the doping levels extracted from the EDX data. Furthermore, a uniform density of states $D_{it} = 3.4 \times 10^{13}$ cm^{-2} was included in the MoS_2 bandgap to model the presence of traps at the interface with SiO_2. The simulation results for the I_{ds}–V characteristics and for the Arrhenius plot are compared with the corresponding experimental data in Figure 4b,c, respectively. The plots show that our numerical model closely reproduces the dependence of the current on both the back-gate voltage and the bias voltage, for temperatures sufficiently close to 300 K and higher. The deviations of the experimental Arrhenius curves from the exponential behavior for temperatures $\lesssim$250 K are likely due to disorder-induced fluctuations of the Schottky barrier height along the NbS_2–MoS_2 interface.[43] This effect is not taken into account in our simulations. Figure 4f shows the local density of states along the device close to flat band conditions. According to the map, the corresponding Schottky barrier height turns out to be $\Phi_B^{FB} \approx 230$ meV.

3. Conclusion

One-step MOCVD method was utilized to synthesize NbS_2–MoS_2 lateral heterostructures with Nb dopants present in monolayer MoS_2. A visible interface and high quality of the as-grown heterostructures were proven by detailed characterization. Due to the increased hole concentration from Nb doping, monolayer MoS_2 shows a p-type transfer characteristic with a high on/off current ratio of $\approx 10^4$. A detailed compositional model of the heterojunction interface, describing the transition between the pure lattice-mismatched phases of NbS_2 and MoS_2 through a buffer phase of 8.3% Nb-doped MoS_2 was derived through DFT simulations. Furthermore, a value of 230 meV for the Schottky barrier height at the NbS_2–MoS_2 interface was estimated by fitting the electrical measurements with the results of self-consistent quantum transport simulations. Our work makes an instructive combination of substitutional doped TMDC materials and 2D metal–semiconductor heterostructures, and paves the way to designing innovative nanoscale devices and CMOS-like 2D circuits.

4. Experimental Section

Material Synthesis: NbS_2–MoS_2 lateral heterostructures were produced by metal–organic chemical vapor deposition (MOCVD) method in the home-built system shown in Figure 1a. Niobium chloride ($NbCl_5$) was chosen as the Nb precursor because of its low melting point and relatively high solubility compared to other precursors (e.g., Nb_2O_5). The Mo precursor, $Mo(CO)_6$, was stored inside of a bubbler whose temperature was maintained at 20 °C. Sodium chloride (NaCl) was used to reduce growth temperature by suppressing the reaction energy barrier.[44] A *c*-plane sapphire substrate was annealed in air for 6 h and spin-coated with 0.3 mol L^{-1} NaCl solution in deionized water as well as 0.00125 mol L^{-1} $NbCl_5$ solution in isopropanol (IPA) before being loaded into the chamber. During the growth process, MoS_2 was synthesized first at 850 °C with 5 sccm of H_2S and 10 sccm of Ar, which carries $\approx 1.8 \times 10^{-4}$ sccm of $Mo(CO)_6$ flowing into the tube. A flow of 4 sccm of H_2 was introduced into the growth chamber to efficiently remove carbon contamination generated from $Mo(CO)_6$. MoS_2 growth lasted for 10 min and the precursor supply was abruptly cut-off. Subsequently, the tube was heated up to 950 °C, and then 35 sccm of H_2S was introduced into the tube for 30 min to react with pre-coated $NbCl_5$ and form NbS_2–MoS_2 heterostructures. Last, the furnace cooled down to room temperature naturally with a mixture gas flow of 5 sccm of H_2S and 200 sccm of Ar in order to provide a sulfur-rich environment. The growth environment was maintained at atmospheric pressure during the whole process.

Raman and Photoluminescence (PL) Measurements: Raman and PL measurements were conducted by using a Renishaw inVia Confocal Raman microscope at room temperature. A laser beam with wavelength of 532 nm and a power of 1 mW was utilized to excite the samples. To obtain suitable spectral ranges and resolution, diffraction gratings of 3000 g mm^{-1} and 300 g mm^{-1} were employed in Raman and PL measurements, respectively.

Sample Transfer: To transfer as-grown heterostructures from the sapphire substrate, the sample was spin-coated with poly(methyl methacrylate) (PMMA) 4% in anisole (A4) at a speed of 2000 rpm for 1 min and baked on a hot plate at 70 °C for 15 min for drying. The edges of the PMMA film were scratched by a sharp tweezer and then the sample was immersed in water for 5 min. Subsequently, the PMMA film attached with heterostructure samples was detached from sapphire by water tension and picked up by the target chip. In order to promote the adhesion, the sample was baked again on a hot plate at 70 °C for 15 min. At last, the sample was immersed in acetone overnight and annealed in high vacuum at 250 °C for 6 h to remove the PMMA residue.

Scanning Transmission Electron Microscopy Measurements: Scanning transmission electron microscopy experiments were conducted using a double aberration-corrected FEI Titan Themis, equipped with a X-FEG, Super-X EDX detector, and a Wein-type monochromator, operated at 80 kV acceleration voltage. All STEM images were acquired using the following conditions: the probe convergence angle was set to 20 mrad, camera length was chosen to be 185 mm which corresponds to the high-angular annular dark field (HAADF) detector 49.5–198 mrad collection angle, the estimated probe current of ≈16–20 pA, and images were recorded with a resolution of 512 × 512 pixels and 8 µs dwell times. EDX measurements were performed in both Titan Themis and FEI Talos TEM. The intensities of STEM-EDS elemental maps and spectrum shown in Figures S1 and S3 (Supporting Information) were recorded using Nb Lα, Mo Kα, and S Kα X-ray emissions, respectively. Velox software, ThermoFisher Scientific was used to process the EDX spectrum and elemental mapping data. Band pass and Inverse fast Fourier transform filtering was used to process the images in ImageJ. Multislice algorithm-based ADF-STEM simulations were carried out with the QSTEM software package using the DFT calculated Nb-MoS_2 atomic model.

Device Fabrication: The heterostructure samples were transferred on Si/SiO_2 substrate before fabrication. The sample was first etched into a suitable geometry by using e-beam lithography and XeF_2 etching. A second step of e-beam lithography was used to make electrode patterns and a layer composed of 2 nm/80 nm-thick Ti/Au was thermally evaporated as electrodes. Finally, a lift-off process was performed in acetone to remove PMMA layer.

Transport Measurements: Electrical transport measurements were carried out in a Janis closed-cycle cryogen-free cryostat. Prior to measurements, the sample was annealed in high vacuum at 150 °C for 6 h. DC electrical measurements were done by applying DC source–drain voltage and back-gate voltage with Agilent E5270B sourcemeter

while measuring four-probe DC voltage and current with Keithley 6514 electrometer.

DFT Simulations: Density-functional theory (DFT) simulations were performed using the Quantum Espresso (QE) package,[45] using 50 Ry as energy cutoff for the wave function and 500 Ry as density cutoff, and $1 \times 22 \times 1$ Monkhorst–Pack k-meshes to sample the Brillouin zone. A plane-wave basis set, a gradient-corrected exchange-correlation (XC) functional (Perdew–Burke–Ernzerhof (PBE)),[46] and scalar-relativistic ultrasoft pseudopotentials (US-PPs) were utilized for all atoms, and also to produce "mixed" pseudopotentials within the virtual crystal approximation (VCA).[38]

Transport Simulation: Transport simulations were performed within the ballistic non-equilibrium Green's function framework, by using the self-consistent Schrödinger–Poisson solver NanoTCAD ViDES.[47] Periodic boundary conditions were applied in the direction transverse to transport, and a set of 30 transverse wave vectors was used to sample the first irreducible Brillouin zone.

The effect of the parasitic sheet resistance R_s was taken into account by replacing in simulations the experimental value of the source-to-drain bias V with $V' = V - R_s I_{ds}$. The latter represents a further equation to be self-consistently coupled to the transport and Poisson equations.

Supporting Information

Supporting Information is available from the Wiley Online Library or from the author.

Acknowledgements

The authors acknowledge the help of Z. Benes (CMI) with electron-beam lithography. Device fabrication was carried out at the EPFL Center for micro and nanotechnology. Electron microscopy imaging was performed at the EPFL Interdisciplinary Centre for Electron Microscopy. This work was financially supported by the European Union's Horizon 2020 research and innovation program under grant agreements No 829035 (QUEFORMAL) and No 785219 and 881603 (Graphene Flagship Core 2 and Core 3), European Research Council (grants no. 682332 and 899775), the Swiss National Science Foundation (grants no. 175822 and 157739) and the CCMX Materials Challenge grant "Large area growth of 2D materials for device integration". Computational support from Cineca Supercomputing Center (Italy) is gratefully acknowledged.

Open access funding provided by Ecole Polytechnique Federale de Lausanne.

Conflict of Interest

The authors declare no conflict of interest.

Author contributions

A.K. initiated and supervised the project. Z.W. performed MOCVD growth with supervision of A.R. M.T. performed STEM measurements and EDX spectroscopy. Z.W. performed Raman and PL measurements with help of Y.Z. Z.W. fabricated the devices and performed electrical measurements with assistance of G.M.M. G.I. designed and supervised the numerical simulation of transport. G.L, F.M., and D.L. developed the quantum transport model, performed the device numerical simulations, and extracted the Schottky barrier height and the MoS_2 series resistance. A.F. performed conception and design of QM modelling. Z.G. and P.K. conducted QM simulations and modelling under supervision of L.S. A.K. and Z.W. analysed the experimental data with input from H.G.J. and M.T. All the authors contributed to the writing of the manuscript.

Data Availability Statement

The data that support the findings of this study are openly available in Zenodo at https://doi.org/10.5281/zenodo.7382708, reference number 7382708.

Keywords

metal–organic chemical vapor deposition (MOCVD), p-type MoS_2, substitutional doping, TMDC heterostructures

Received: October 11, 2022
Revised: December 30, 2022
Published online:

[1] B. Radisavljevic, A. Radenovic, J. Brivio, V. Giacometti, A. Kis, *Nat. Nanotechnol.* **2011**, *6*, 147.
[2] S. W. Han, H. Kwon, S. K. Kim, S. Ryu, W. S. Yun, D. H. Kim, J. H. Hwang, J.-S. Kang, J. Baik, H. J. Shin, S. C. Hong, *Phys. Rev. B* **2011**, *84*, 045409.
[3] S. Manzeli, D. Ovchinnikov, D. Pasquier, O. V. Yazyev, A. Kis, *Nat. Rev. Mater.* **2017**, *2*, 1733.
[4] A. Splendiani, L. Sun, Y. Zhang, T. Li, J. Kim, C.-Y. Chim, G. Galli, F. Wang, *Nano Lett.* **2010**, *10*, 1271.
[5] K. F. Mak, C. Lee, J. Hone, J. Shan, T. F. Heinz, *Phys. Rev. Lett.* **2010**, *105*, 136805.
[6] K. Dolui, I. Rungger, S. Sanvito, *Phys. Rev. B* **2013**, *87*, 165402.
[7] B. Akdim, R. Pachter, S. Mou, *Nanotechnology* **2016**, *27*, 185701.
[8] G. Migliato Marega, Y. Zhao, A. Avsar, Z. Wang, M. Tripathi, A. Radenovic, A. Kis, *Nature* **2020**, *587*, 72.
[9] P. Yao, H. Wu, B. Gao, J. Tang, Q. Zhang, W. Zhang, J. J. Yang, H. Qian, *Nature* **2020**, *577*, 641.
[10] T. kumar Agarwal, B. Soree, I. Radu, P. Raghavan, G. Iannaccone, G. Fiori, W. Dehaene, M. Heyns, *Sci. Rep.* **2017**, *7*, 5016.
[11] G. Iannaccone, F. Bonaccorso, L. Colombo, G. Fiori, *Nat. Nanotechnol.* **2018**, *13*, 183.
[12] S. Chuang, C. Battaglia, A. Azcatl, S. McDonnell, J. S. Kang, X. Yin, M. Tosun, R. Kapadia, H. Fang, R. M. Wallace, A. Javey, *Nano Lett.* **2014**, *14*, 1337.
[13] S. Wu, Y. Zeng, X. Zeng, S. Wang, Y. Hu, W. Wang, S. Yin, G. Zhou, W. Jin, T. Ren, Z. Guo, J. Lu, *2D Mater.* **2019**, *6*, 025007.
[14] A. Azcatl, X. Qin, A. Prakash, C. Zhang, L. Cheng, Q. Wang, N. Lu, M. J. Kim, J. Kim, K. Cho, R. Addou, C. L. Hinkle, J. Appenzeller, R. M. Wallace, *Nano Lett.* **2016**, *16*, 5437.
[15] A. Nipane, D. Karmakar, N. Kaushik, S. Karande, S. Lodha, *ACS Nano* **2016**, *10*, 2128.
[16] S.-W. Min, M. Yoon, S. J. Yang, K. R. Ko, S. Im, *ACS Appl. Mater. Interfaces* **2018**, *10*, 4206.
[17] S. Zhang, S. T. Le, C. A. Richter, C. A. Hacker, *Appl. Phys. Lett.* **2019**, *115*, 073106.
[18] M. Li, J. Yao, X. Wu, S. Zhang, B. Xing, X. Niu, X. Yan, Y. Yu, Y. Liu, Y. Wang, *ACS Appl. Mater. Interfaces* **2020**, *12*, 6276.
[19] E. Z. Xu, H. M. Liu, K. Park, Z. Li, Y. Losovyj, M. Starr, M. Werbianskyj, H. A. Fertig, S. X. Zhang, *Nanoscale* **2017**, *9*, 3576.
[20] B. Song, H. Gu, M. Fang, Z. Guo, Y.-T. Ho, X. Chen, H. Jiang, S. Liu, *ACS Appl. Electron. Mater.* **2021**, *3*, 2564.
[21] Y. C. Cheng, Z. Y. Zhu, W. B. Mi, Z. B. Guo, U. Schwingenschlögl, *Phys. Rev. B* **2013**, *87*, 100401.
[22] A. Ramasubramaniam, D. Naveh, *Phys. Rev. B* **2013**, *87*, 195201.
[23] Y. Liu, P. Stradins, S.-H. Wei, *Sci. Adv.* **2016**, *2*, e1600069.
[24] X. Liu, M. C. Hersam, *Adv. Mater.* **2018**, *30*, 1801586.
[25] A. K. Geim, I. V. Grigorieva, *Nature* **2013**, *499*, 419.

[26] K. L. Choy, *Prog. Mater. Sci.* **2003**, *48*, 57.
[27] Y. Gong, J. Lin, X. Wang, G. Shi, S. Lei, Z. Lin, X. Zou, G. Ye, R. Vajtai, B. I. Yakobson, H. Terrones, M. Terrones, B. K. Tay, J. Lou, S. T. Pantelides, Z. Liu, W. Zhou, P. M. Ajayan, *Nat. Mater.* **2014**, *13*, 1135.
[28] X. Duan, C. Wang, J. C. Shaw, R. Cheng, Y. Chen, H. Li, X. Wu, Y. Tang, Q. Zhang, A. Pan, J. Jiang, R. Yu, Y. Huang, X. Duan, *Nat. Nanotechnol.* **2014**, *9*, 1024.
[29] Y. Zhang, L. Yin, J. Chu, T. A. Shifa, J. Xia, F. Wang, Y. Wen, X. Zhan, Z. Wang, J. He, *Adv. Mater.* **2018**, *30*, 1803665.
[30] H. Kim, D. Ovchinnikov, D. Deiana, D. Unuchek, A. Kis, *Nano Lett.* **2017**, *17*, 5056.
[31] Z. Wang, C.-Y. Cheon, M. Tripathi, G. M. Marega, Y. Zhao, H. G. Ji, M. Macha, A. Radenovic, A. Kis, *ACS Nano* **2021**, *15*, 18403.
[32] H. Heo, J. H. Sung, G. Jin, J.-H. Ahn, K. Kim, M.-J. Lee, S. Cha, H. Choi, M.-H. Jo, *Adv. Mater.* **2015**, *27*, 3803.
[33] A. Sohn, C. Kim, J.-H. Jung, J. H. Kim, K.-E. Byun, Y. Cho, P. Zhao, S. W. Kim, M. Seol, Z. Lee, S.-W. Kim, H.-J. Shin, *Adv. Mater.* **2022**, *34*, 2103286.
[34] R. Rao, A. E. Islam, S. Singh, R. Berry, R. K. Kawakami, B. Maruyama, J. Katoch, *Phys. Rev. B* **2019**, *99*, 195401.
[35] A. Michail, N. Delikoukos, J. Parthenios, C. Galiotis, K. Papagelis, *Appl. Phys. Lett.* **2016**, *108*, 173102.
[36] S. Mouri, Y. Miyauchi, K. Matsuda, *Nano Lett.* **2013**, *13*, 5944.
[37] K. F. Mak, K. He, C. Lee, G. H. Lee, J. Hone, T. F. Heinz, J. Shan, *Nat. Mater.* **2013**, *12*, 207.
[38] O. de la Peña, A. Aguayo, R. de Coss, *Phys. Rev. B* **2002**, *66*, 012511.
[39] T. Cusati, G. Fiori, A. Gahoi, V. Passi, M. C. Lemme, A. Fortunelli, G. Iannaccone, *Sci. Rep.* **2017**, *7*, 5109.
[40] R. Das, B. Rakshit, S. Debnath, P. Mahadevan, *Phys. Rev. B* **2014**, *89*, 115201.
[41] F. A. Rasmussen, K. S. Thygesen, *J. Phys. Chem. C* **2015**, *119*, 13169.
[42] S. K. Cheung, N. W. Cheung, *Appl. Phys. Lett.* **1986**, *49*, 85.
[43] H. Altuntaş, Ş. Altındal, H. Shtrikman, S. Özçelik, *Microelectron. Reliab.* **2009**, *49*, 904.
[44] P. Yang, X. Zou, Z. Zhang, M. Hong, J. Shi, S. Chen, J. Shu, L. Zhao, S. Jiang, X. Zhou, Y. Huan, C. Xie, P. Gao, Q. Chen, Q. Zhang, Z. Liu, Y. Zhang, *Nat. Commun.* **2018**, *9*, 979.
[45] P. Giannozzi, S. Baroni, N. Bonini, M. Calandra, R. Car, C. Cavazzoni, D. Ceresoli, G. L. Chiarotti, M. Cococcioni, I. Dabo, A. Dal Corso, S. de Gironcoli, S. Fabris, G. Fratesi, R. Gebauer, U. Gerstmann, C. Gougoussis, A. Kokalj, M. Lazzeri, L. Martin-Samos, N. Marzari, F. Mauri, R. Mazzarello, S. Paolini, A. Pasquarello, L. Paulatto, C. Sbraccia, S. Scandolo, G. Sclauzero, A. P. Seitsonen, et al., *J. Phys.: Condens. Matter* **2009**, *21*, 395502.
[46] J. P. Perdew, K. Burke, M. Ernzerhof, *Phys. Rev. Lett.* **1996**, *77*, 3865.
[47] G. Fiori, G. Iannaccone, *Proc. IEEE* **2013**, *101*, 1653.